



Controlling optical field collapse by elliptical symmetry hybrid polarization structure

DAN WANG,¹ YUE PAN,¹ JIA-QI LÜ,¹ PING-PING LI,¹ GUI-GENG LIU,¹ MENG-QIANG CAI,¹
YONGNAN LI,¹ CHENGHOU TU,^{1,4} AND HUI-TIAN WANG^{1,2,3,*}

¹School of Physics and MOE Key Laboratory of Weak Light Nonlinear Photonics, Nankai University, Tianjin 300071, China

²National Laboratory of Solid State Microstructures and School of Physics, Nanjing University, Nanjing 210093, China

³Collaborative Innovation Center of Advanced Microstructures, Nanjing University, Nanjing 210093, China

⁴e-mail: tuchenghou@nankai.edu.cn

*Corresponding author: htwang@nju.edu.cn

Received 24 May 2018; revised 7 August 2018; accepted 10 August 2018; posted 14 August 2018 (Doc. ID 332334); published 7 September 2018

Engineering the diversity of the spatial structure of polarization states offers a new approach to produce controllable and designable filament patterns. Here we predict theoretically and demonstrate experimentally the novel collapsing behaviors of the optical fields by using the elliptical symmetry hybrid polarization structure in a self-focusing Kerr medium. The results reveal that the distribution of the hybrid polarization states, the spin angular momentum (SAM) gradient, and the collapsing patterns could be manipulated by changing the eccentricity, the topological charge, and the initial phase of the optical field. Owing to the synergy of the hybrid polarization states and its spatial symmetry, the collapsing behaviors are controllable, and have the robust feature insensitive to the random noise. Our idea may offer an alternative route to produce the controllable and robust multiple filamentation in other nonlinear systems, thereby facilitating the development of additional surprising applications. © 2018 Optical Society of America

<https://doi.org/10.1364/JOSAB.35.002373>

1. INTRODUCTION

Field collapse, which occurs in many physical systems including optics, fluidics, plasma, and Bose–Einstein condensates, has attracted much attention, owing to its universality, complexity, and applicability [1–6]. A femtosecond (fs) optical field could undergo the collapse in a self-focusing Kerr medium under the input power beyond a certain critical power. As the collapse aggravates, there will occur the higher-order nonlinearity, which combines with the intrinsic diffraction of the optical field to counterbalance the self-focusing effect, resulting ultimately in the filamentation [7–13]. In general, the filamentation patterns are initialized from the unpredictable symmetry breaking caused by the random noise, making it to be hardly controlled.

However, it is always anticipated for the realization of controllable field collapse and sequent filamentation, due to its practical applications, such as guiding microwave radiation [14], enhancement of terahertz emission [15], generation of millijoule-level supercontinuum in solid media [16], etc. For those purposes, some methods have been proposed by controlling the input power and divergence angle [17], shaping the field profile [18,19], using the amplitude/phase mask [20–23], and introducing the spatial regularization [24]. In fact, the above methods are to manipulate the spatial structure of scalar

optical fields in phase and amplitude, whereas the spatial structure of polarization states was rarely involved.

Polarization, as an intrinsic and fundamental vectorial nature of light, plays an indispensable role in the light–matter interaction. We first utilized the hybrid polarized vector optical fields (VOFs) to realize the controllable and designable filamentation [25,26], in which the symmetry of light–matter nonlinear interaction is actively broken by introducing the polarization-state-dependent refractive index change. However, the diversity of the spatial geometry of polarization states is not yet applied fully. Inasmuch as the hybrid polarized VOFs in [25,26] are only a special case, in which the polarization states exhibit a cylindrical symmetry or the ellipticity (or spin angular momentum, SAM) of the polarization states is a sin/cos function of the azimuthal angle. A question is raised that whether the azimuthally inhomogeneous distribution of hybrid polarization states in the field cross section, as a new approach, can be used to effectively control the field collapse and the sequent multiple filamentation. The generalized hybrid polarized vector fields, which break the cylindrical symmetry of the polarization states of the VOFs, become an interesting approach to control the filamentation.

Here we present an idea that the actively controllable collapsing patterns are achieved by designing the geometric

configurations of the initial hybrid polarization states. One of the simplest methods is to design and generate a new kind of elliptic-symmetry azimuthally variant hybrid polarized VOFs (ES-AV-HP-VOFs) to explore how the fields collapse and the sequent multiple filamentation. The eccentricity, describing the elliptic geometry of the spatial hybrid polarization states, provides an additional degree of freedom assisting in engineering the azimuthally variant gradient of the hybrid polarization states and controlling the collapsing patterns. Besides the intensity, the contribution of the polarization states to the nonlinear refractive index change strongly affects the nonlinear dynamic property of the structured optical fields.

2. THEORY

An ES-AV-HP-VOF can be written as

$$\mathbf{E} = A(r)(\cos \delta \hat{\mathbf{e}}_H + j \sin \delta \hat{\mathbf{e}}_V), \quad (1)$$

where $\hat{\mathbf{e}}_H$ and $\hat{\mathbf{e}}_V$ are the orthogonally horizontal and vertical unit vectors in the Cartesian coordinate system; $A(r)$ represents the radially variant amplitude in the cross section of the ES-AV-HP-VOF and has a top-hat-like profile with a radius of r_0 excluding a polarization singularity at the center; and $\delta = m\varphi + \delta_0$ (m is the topological charge and δ_0 is the initial phase), respectively. In particular, φ is not the azimuthal angle in the polar coordinate system and $\varphi = \arctan(a^2 y/b^2 x) = \arctan(a^2 \tan \phi/b^2) = \arctan(a^2 \sqrt{1-x^2/a^2}/bx)$, which is derived from the elliptic equation $x^2/a^2 + y^2/b^2 = 1$ ($a > b > 0$), where a and b are the semi-major axis and semi-minor axis of the ellipse, respectively. ϕ ($\tan \phi = y/x$) is the azimuthal angle in the polar coordinate system attached to the cross section of the ES-AV-HP-VOF described by Eq. (1). One should point out that when $\varepsilon = 0$ or $a = b$, φ degenerates into ϕ , i.e., $\varphi = \phi$. The eccentricity ε of an ES-AV-HP-VOF is described by $\varepsilon = \sqrt{1 - b^2/a^2}$ with a range of $\varepsilon \in [0, 1]$. Thus the eccentricity ε could provide an additional degree of freedom to control the azimuthal distribution of hybrid polarization states and the field collapsing behavior.

As is well known, the polarization of the optical field associates with the optical SAM. For the ES-AV-HP-VOF described by Eq. (1), its local SAM should be $\sigma\hbar$ with $\sigma = S_3$, where S_3 is a normalized Stokes parameter in the representation

of Poincaré sphere for describing the polarization states. $\sigma = S_3 = +1$ and $\sigma = S_3 = -1$ correspond to the right-handed (RH) and left-handed (LH) circular polarizations, while $\sigma = S_3 = 0$ indicates the linear polarization, respectively. Based on the definition of the Stokes parameter, S_3 of the ES-AV-HP-VOF described by Eq. (1) should be

$$\begin{aligned} S_3(\phi) &= \sigma(\phi) = \sin(2\delta) = \sin(2m\varphi + 2\delta_0) \\ &= \sin[2m \arctan(a^2 \tan \phi/b^2) + 2\delta_0]. \end{aligned} \quad (2)$$

S_3 or the polarization state (SAM, $\sigma\hbar$) depends on the azimuthal angle ϕ while independent of the radial coordinate. For the case of $\varepsilon = 0$ or $a = b$, the polarization state (SAM) is a sine function of ϕ as

$$S_3(\phi)|_{\varepsilon=0} = \sigma(\phi)|_{\varepsilon=0} = \sin(2m\phi + 2\delta_0). \quad (3)$$

Figure 1 shows the distribution of the polarization state (SAM) of the ES-AV-HP-VOF ($m = 1$, $\delta_0 = 0$, and $\delta_0 = \pi/4$) with different eccentricities of $\varepsilon = 0, 0.3, 0.6, 0.8$. When $\varepsilon \neq 0$, the distribution geometry of the hybrid polarization states (as shown by the red arrows) exhibits a set of concentric ellipses (as shown by the black dashed ellipses) with the same eccentricity. Meanwhile, when $\varepsilon = 0$, the ES-AV-HP-VOF degenerates into the cylindrical-symmetry azimuthally variant hybrid polarized VOF (CS-AV-HP-VOF) [27]. The black background corresponds to the zero SAM or the linear polarization, the green (yellow) background indicates the $+\hbar$ ($-\hbar$) SAM or the RH (LH) circular polarization, and the black \Rightarrow green (black \Rightarrow yellow) gradual color background represents the $0 < \sigma\hbar < +\hbar$ ($0 > \sigma\hbar > -\hbar$) SAM or the RH (LH) elliptical polarization. One can be seen that the variation of the polarization state (SAM, $\sigma\hbar$) in the azimuthal direction becomes more inhomogeneous as ε increases. In the vicinity of $\phi = 0$ and $\phi = \pi$ ($\phi = \pi/2$ and $\phi = 3\pi/2$) directions, in detail, the variation of the polarization state becomes faster (slower) as ε increases.

To theoretically explore the nonlinear propagation behavior of an ES-AV-HP-VOF in the isotropic Kerr medium, a (2 + 1)-dimensional vector-version nonlinear-Schrödinger (NLS) equation should be used. Under the slowly varying amplitude approximation, the NLS equation can be divided into a

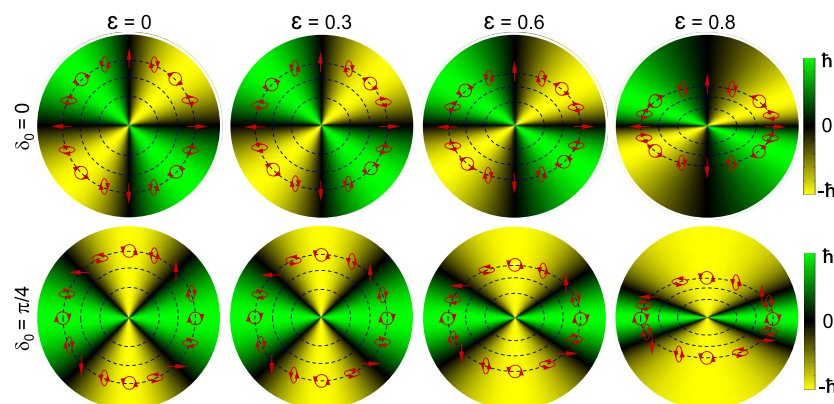


Fig. 1. Schematic distributions of the polarization states and the SAM for the ES-AV-HP-VOFs with $m = 1$ and $\delta_0 = 0$ for different eccentricities ($\varepsilon = 0, 0.3, 0.6, 0.8$).

pair of coupled NLS equations for two orthogonal components as follows:

$$\frac{\partial \psi_H}{\partial \zeta} = \frac{j}{4} \nabla_{\perp}^2 \psi_H + \frac{j\alpha P}{3P_C} (3|\psi_H|^2 \psi_H + 2|\psi_V|^2 \psi_H + \psi_V^2 \psi_H^*), \quad (4)$$

$$\frac{\partial \psi_V}{\partial \zeta} = \frac{j}{4} \nabla_{\perp}^2 \psi_V + \frac{j\alpha P}{3P_C} (3|\psi_V|^2 \psi_V + 2|\psi_H|^2 \psi_V + \psi_H^2 \psi_V^*), \quad (5)$$

where ψ_q ($q = H, V$) is the dimensionless q -component normalized by the total field as

$$\psi_q(\rho, \phi; \zeta) = \frac{E_q(\rho, \phi; \zeta)}{\sqrt{\iint [|E_H(\rho, \phi; \zeta)|^2 + |E_V(\rho, \phi; \zeta)|^2] \rho d\rho d\phi}}.$$

Here $P = 2n_0\epsilon_0 c \iint [|E_H(\rho, \phi; \zeta)|^2 + |E_V(\rho, \phi; \zeta)|^2] \rho d\rho d\phi$ is the power and $P_C = \alpha\lambda^2/4\pi n_0 n_2$ is the critical power for self-focusing, respectively. $\rho = r/r_0$ and $\zeta = z/L_d$ ($L_d = \pi r_0^2/\lambda$) are the dimensionless cylindrical coordinates, n_0 and n_2 are the linear and nonlinear refractive indices of the Kerr medium, α is a constant dependent on the initial field shape [28], c is the speed of light in vacuum, and λ is the wavelength of light, respectively. On the right-hand side of Eqs. (4) and (5), the first term represents the contribution from the diffraction described by the transverse Laplacian $\nabla_{\perp}^2 = \partial^2/\partial\rho^2 + \rho^{-1}\partial/\partial\rho + \rho^{-2}\partial^2/\partial\phi^2$ and the second term is from the Kerr nonlinearity.

3. NUMERICAL SIMULATION

The ES-AV-HP-VOF might have some properties more useful than the CS-AV-HP-VOF, because it has an additional controllable degree of freedom (eccentricity ϵ) and the distribution diversity of hybrid polarization states. Here we focus on their collapsing behaviors in the self-focusing Kerr medium. Under $P = 10P_C$, a large number of simulations are performed by the beam propagation method [29], which is used to numerically solve Eq. (4). When the spatial random noise is added for simulations, we keep the random noise with a level of 10% in amplitude, which follows a uniform distribution within a range of 10%.

A. ES-AV-HP-VOFs ($m = 1, \delta_0 = 0$)

First, the collapsing behaviors of the ES-AV-HP-VOFs ($m = 1, \delta_0 = 0$) with different eccentricity ϵ in the Kerr medium are studied, as shown in Fig. 2. The initial input field is pre-focused on the input face of the Kerr medium (i.e., the focal plane is in the Kerr medium). Although all the initial input ES-AV-HP-VOFs have the top-hat-like profile in intensity excluding the central polarization singularity, the pre-focused fields incident on the input plane of the Kerr medium are different, as the simulated patterns shown in the first column of Fig. 2, due to the different ϵ .

Here we classify into the two cases based on the value of ϵ : $\epsilon = 0$ and $\epsilon \neq 0$. For the case of $\epsilon = 0$, the collapsing evolutions simulated by Eqs. (4) and (5) are shown in the first and second rows of Fig. 2. In this case, the ES-AV-HP-VOF

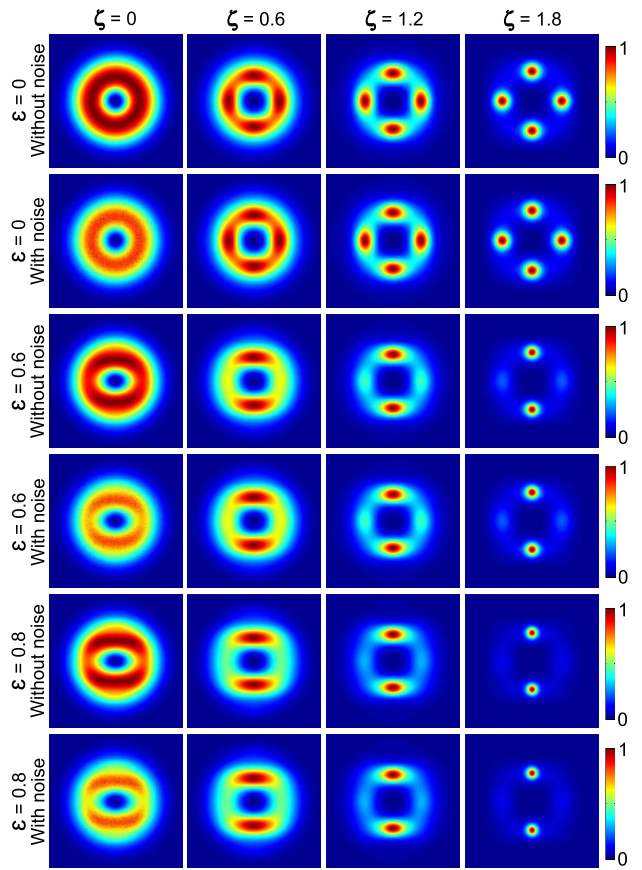


Fig. 2. Simulated nonlinear propagation behaviors of the ES-AV-HP-VOFs ($m = 1, \delta_0 = 0$) with different ϵ ($= 0, 0.6, 0.8$) in the Kerr medium. The first and second rows show the cases without and with random noise ($\epsilon = 0$), respectively. For comparison, the ES-AV-HP-VOFs ($\epsilon \neq 0$) without and with random noise are also shown in the third and fourth rows for the case of $\epsilon = 0.6$ and in the fifth and sixth rows for the case of $\epsilon = 0.8$. The four columns (from left to right) correspond to four propagation distances ($\zeta = 0, 0.6, 1.2, 1.8$).

degenerates into a CS-AV-HP-VOF. The four deterministic collapsing patterns produced by the CS-AV-HP-VOF ($m = 1, \delta_0 = 0$) are located at the azimuthal locations of $\phi = 0, \pi/2, \pi, 3\pi/2$, which is in agreement with [25]. For the case of $\epsilon \neq 0$, including $\epsilon = 0.6$ (third and fourth rows) and $\epsilon = 0.8$ (fifth and sixth rows) in Fig. 2, (i) the larger ϵ leads to the axial-symmetry breaking behaviors by changing the eccentricity of the input field; (ii) the ES-AV-HP-VOFs ($m = 1, \delta_0 = 0$) collapse to converge into the two (instead of four) deterministic filaments located at $\phi = \pi/2, 3\pi/2$, corresponding to the linear polarization in the semi-minor axis of the ellipse; and (iii) the collapsing patterns are insensitive to the random noise.

To clearly show the evolution of azimuthal-variant polarization states during the collapsing of ES-AV-HP-VOFs ($m = 1, \delta_0 = 0$) with $\epsilon = 0$ and $\epsilon \neq 0$ in the isotropic Kerr medium, we simulate the Stocks parameter S_3 , as shown in Fig. 3. For the case of $\epsilon = 0$, S_3 of the initial input field obeys $S_3(\phi) = \sin(2\phi)$, shown by the black curve in Fig. 3(a); as the propagation distance increases, $|S_3|$ of the local

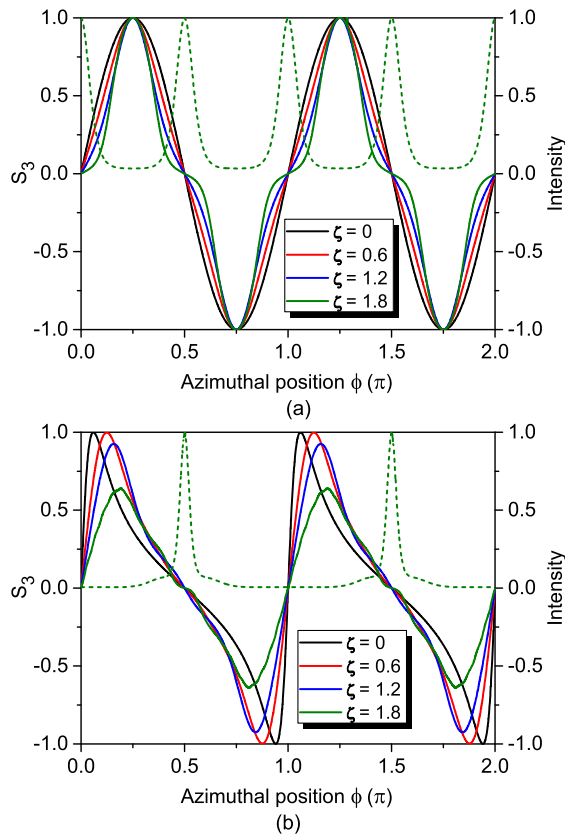


Fig. 3. Simulated evolution S_3 of the azimuthal-variant polarization states for the ES-AV-HP-VOFs ($m = 1, \delta_0 = 0$) with different eccentricity. (a) $\varepsilon = 0$ and (b) $\varepsilon = 0.8$.

polarization state has a tendency to decrease by the coupling between the two orthogonally polarized components in the Kerr medium, as shown by the other three curves in Fig. 3(a). For the case of $\varepsilon = 0.8$, S_3 of the initial input field obeys $S_3(\phi) = \sin[2m \arctan(\tan \phi / 0.36)]$, shown by the black curve in Fig. 3(b); however, the nonlinear coupling does not always lead to the decrease of $|S_3|$ of the local polarization state, which is different from Fig. 3(a). Interestingly, for both cases of $\varepsilon = 0$ and $\varepsilon \neq 0$, so long as $\delta_0 = 0$ the local polarization states have no change to keep the initial linear polarization at four special azimuthal locations of $\phi(n) = n\pi/2$ ($n = 0, 1, 2, 3$). For the case of $\varepsilon = 0$, the nonlinear coupling also does not result in the change of the azimuthal locations for the initial circular polarization ($|S_3| = 1$); while for the case of $\varepsilon \neq 0$, the nonlinear coupling results in the shift of the azimuthal locations for the initial circular polarization ($|S_3| = 1$). After comparing Fig. 3 with Fig. 2, we find that the final filaments could occur at those azimuthal locations, in which the initial polarization states are linearly polarized; in particular, they are more favorite to occur at the linearly polarized locations, which have the smaller azimuthal gradient ($|\partial S_3 / \partial \phi|$) of S_3 . For instance, for the case of $\varepsilon = 0.8 \neq 0$, the two filaments occur at $\phi = \pi/2$ and $3\pi/2$ instead of $\phi = 0$ and π , because $|\partial S_3 / \partial \phi|_{\phi=\pi/2, 3\pi/2} < |\partial S_3 / \partial \phi|_{\phi=0, \pi}$. In contrast, for the case of $\varepsilon = 0$, the four filaments occur at $\phi(n) = n\pi/2$ ($n = 0, 1, 2, 3$), because $|\partial S_3 / \partial \phi|_{\phi=\pi/2, 3\pi/2} = |\partial S_3 / \partial \phi|_{\phi=0, \pi}$.

B. ES-AV-HP-VOFs ($m = 1, \delta_0 = \pi/4$)

We now change the initial phase δ_0 (within a range of $\delta_0 \in [0, \pi/4]$) of the ES-AV-HP-VOFs ($m = 1$) with different eccentricities of $\varepsilon = 0, 0.6, 0.8$. The collapsing behaviors simulated by Eqs. (4) and (5) are shown in Fig. 4. We also classify into the two cases: $\varepsilon = 0$ and $\varepsilon \neq 0$. For the case of $\varepsilon = 0$, the ES-AV-HP-VOF degenerates into the CS-AV-HP-VOF ($m = 1, \delta_0 = \pi/4$). Clearly, the four deterministic filaments produced by the CS-AV-HP-VOF ($m = 1, \delta_0 = \pi/4$) are counter-clockwise rotated by $\pi/4$ with respect to the CS-AV-HP-VOF ($m = 1, \delta_0 = 0$) shown in Fig. 2, which correspond to the linear polarization. However, when $\varepsilon \neq 0$, new features are found: (i) the filaments do not reduce to two while still keeping to four filaments for any value of ε , which is different from the case ($m = 1, \delta_0 = 0, \varepsilon \neq 0$) of Fig. 2; and (ii) as ε increases, the four filaments are changed from a square for $\varepsilon = 0$ into an elongated rectangle for $\varepsilon \neq 0$.

Meanwhile, we also simulate the evolution of S_3 (or SAM) during the collapsing of ES-AV-HP-VOFs ($m = 1, \delta_0 = \pi/4$)

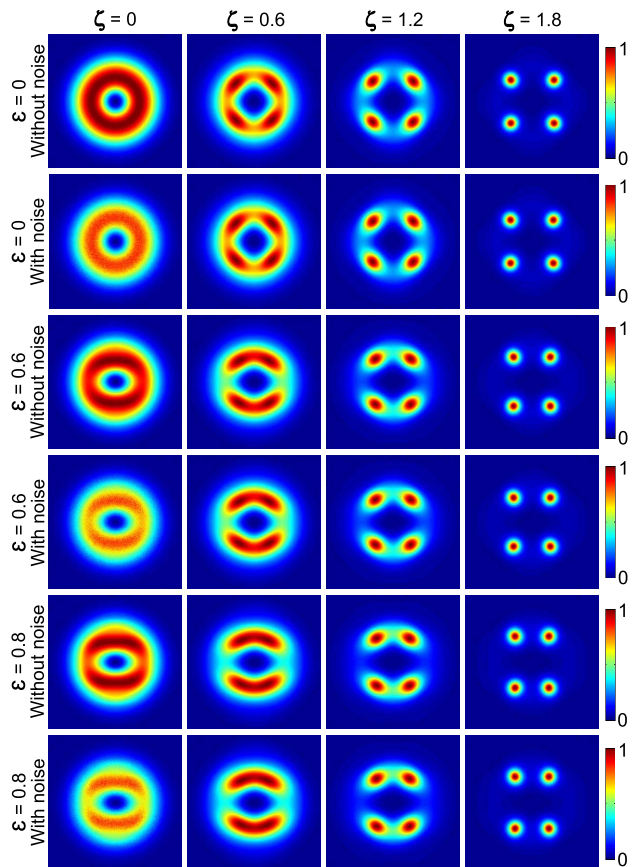


Fig. 4. Simulated nonlinear propagation behaviors of ES-AV-HP-VOFs ($m = 1, \delta_0 = \pi/4$) with the different $\varepsilon (= 0, 0.6, 0.8)$ in the Kerr medium. The first and second rows show the cases without and with random noise ($\varepsilon = 0$), respectively. For comparison, the ES-AV-HP-VOFs ($\varepsilon \neq 0$) without and with random noise are also shown in the third and fourth rows for the case $\varepsilon = 0.6$ and in the fifth and sixth rows for the case $\varepsilon = 0.8$. The four columns (from left to right) correspond to four propagation distances ($\zeta = 0, 0.6, 1.2, 1.8$).

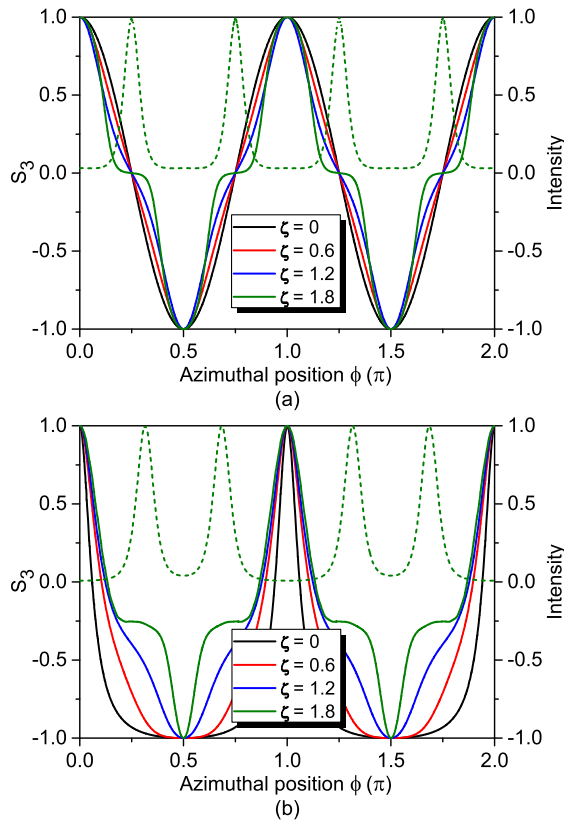


Fig. 5. Simulated evolution S_3 of the azimuthal-variant polarization states for the ES-AV-HP-VOFs ($m = 1, \delta_0 = \pi/4$) with different eccentricity. (a) $\varepsilon = 0$ and (b) $\varepsilon = 0.8$.

with $\varepsilon = 0$ and $\varepsilon \neq 0$ in the Kerr medium, as shown in Figs. 5(a) and 5(b), respectively. For the case of $\varepsilon = 0$, S_3 of the initial input fields obeys $S_3(\phi) = \sin(2\phi + \pi/2)$, shown by the black curve in Fig. 5(a). As shown by the other three curves in Fig. 5(a), the nonlinear coupling results in the decrease of $|S_3|$ of the local polarization state at any azimuthal location. In particular, in eight special azimuthal locations with the linear or circular polarizations, the nonlinear coupling does not cause the change of their polarization states. These features are the same as the case of $\delta_0 = 0$ in Fig. 3(a).

For the case of $\varepsilon = 0.8 \neq 0$, S_3 of the initial input field obeys $S_3(\phi) = \sin[2m \arctan(\tan \phi/0.36) + \pi/2]$, shown by the black curve in Fig. 5(b). As shown by the other three curves, the nonlinear coupling does not always lead to the decrease of $|S_3|$ of the local polarization state, which is the same as Fig. 3(b). However, in four special azimuthal locations with the circular polarizations, the nonlinear coupling does not cause the change of their polarization states, which is different from the case of $\delta_0 = 0$ and $\varepsilon \neq 0$ in Fig. 3(b).

After comparing Fig. 4 with Fig. 5, we find that (i) for $\varepsilon = 0$, the four filaments locate at $\phi(n) = (2n + 1)\pi/4$ ($n = 0, 1, 2, 3$), in which the polarization states are always linearly polarized; and (ii) for $\varepsilon \neq 0$, the filaments do not locate at $\phi(n) = (2n + 1)\pi/4$ ($n = 0, 1, 2, 3$), in which the initial polarization states are not linearly polarized and are changed due to the nonlinear coupling.

C. ES-AV-HP-VOFS ($m = 1, \delta_0 = 3\pi/8$)

Given the ES-AV-HP-VOFs ($m = 1, \delta_0 = 3\pi/8$) with different eccentricities ($\varepsilon = 0, 0.6, 0.8$), we continue to study their collapsing behaviors based on Eqs. (4) and (5), as shown in Fig. 6. For the case of $\varepsilon = 0$, the ES-AV-HP-VOF degenerates into a CS-AV-HP-VOF ($m = 1, \delta_0 = 3\pi/8$), and the simulation results are shown in the first and second rows of Fig. 6. The four deterministic collapsing patterns produced by the CS-AV-HP-VOF ($m = 1, \delta_0 = 3\pi/8$) are counter-clockwise rotated $\pi/8$ with respect to the case ($m = 1, \delta_0 = 0, \varepsilon = 0$) in Fig. 2. Four filaments are located at the azimuthal locations of $\phi = \pi/8, 5\pi/8, 9\pi/8, 13\pi/8$, in which the initial polarization states are linearly polarized. However, when $\varepsilon \neq 0$, including $\varepsilon = 0.6$ (third and fourth rows) and $\varepsilon = 0.8$ (fifth and sixth rows), $\varepsilon \neq 0$ leads to the ES-AV-HP-VOF to collapse two (instead of four) filaments, which is the same as the case ($m = 1, \delta_0 = 0, \varepsilon \neq 0$). The two filaments are located at the azimuthal locations which are very close to but slightly smaller than $\phi = 5\pi/8, 13\pi/8$.

The evolutions of S_3 (or SAM) during the collapsing of ES-AV-HP-VOFs ($m = 1, \delta_0 = 3\pi/8$) with $\varepsilon = 0$ and

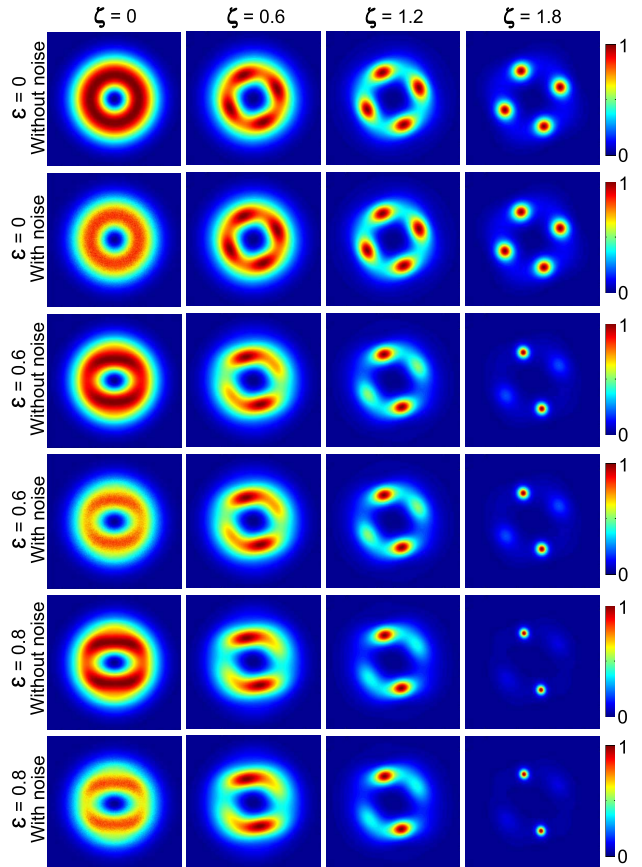


Fig. 6. Simulated nonlinear propagation behaviors of ES-AV-HP-VOFs ($m = 1$ and $\delta_0 = 3\pi/8$) with the different $\varepsilon (= 0, 0.6, 0.8)$ in the Kerr medium. The first and second rows show the cases without and with random noise ($\varepsilon = 0$), respectively. For comparison, the ES-AV-HP-VOFs ($\varepsilon \neq 0$) without and with random noise are also shown in the third and fourth rows for the case $\varepsilon = 0.6$ and in the fifth and sixth rows for the case $\varepsilon = 0.8$. The four columns (from left to right) correspond to four propagation distances ($\zeta = 0, 0.6, 1.2, 1.8$).

$\varepsilon = 0.8 \neq 0$ in the isotropic Kerr medium, are also simulated, as shown in Figs. 7(a) and 7(b), respectively. For the case of $\varepsilon = 0$, S_3 of the initial input fields obeys $S_3(\phi) = \sin(2\phi + 3\pi/4)$, shown by the black curve in Fig. 7(a). As shown by the other three curves in Fig. 7(a), the nonlinear coupling results in the decrease of $|S_3|$ of the local polarization state at any azimuthal location. In particular, in eight special azimuthal locations at $\phi(n) = n\pi/2 + \pi/8$ for linear polarizations and $\phi(n) = n\pi/2 + 3\pi/8$ (where $n = 0, 1, 2, 3$), the nonlinear coupling does not cause the change of their polarization states. These features are the same as the case of $\delta_0 = 0$ in Figs. 3(a) and 5(a).

For the case of $\varepsilon = 0.8 \neq 0$, S_3 of the initial input field obeys $S_3(\phi) = \sin[2m \arctan(\tan \phi/0.36) + 3\pi/4]$, shown by the black curve in Fig. 7(b). As shown by the other three curves, the nonlinear coupling does not always lead to the decrease of $|S_3|$ of the local polarization state, which is the same as Figs. 3(b) and 5(b). However, this case has a completely different feature that the polarization states at all the azimuthal locations are changed by the nonlinear coupling.

After comparing Fig. 6 with Fig. 7, we find that (i) for $\varepsilon = 0$, the four filaments locate at $\phi(n) = n\pi/2 + \pi/8$ (where $n = 0, 1, 2, 3$), in which the polarization states are always linearly polarized; and (ii) for $\varepsilon \neq 0$, the filaments become into two located at the azimuthal locations which are very close to but slightly smaller than $\phi = 5\pi/8, 13\pi/8$, as mentioned above. In particular, at the two azimuthal locations, the final

polarization states after the nonlinear coupling favor to tend to become into the linear polarization.

Finally, we should point out that the dashed curves in Figs. 3, 5, and 7 show the azimuthal intensity distribution after the collapsing of the ES-AV-HP-VOFs, in which the intensity peaks correspond to the locations of the filaments. The purpose is to clearly show the correspondence of filaments with the azimuthal locations and the local polarization states.

4. DISCUSSION

After summarizing all the simulation results, we obtain the following conclusions: (i) ε indeed provides a new degree of freedom for controlling the collapse of the ES-AV-HP-VOFs; (ii) when $\varepsilon = 0$, the ES-AV-HP-VOFs with m always produce $4m$ filaments located at the azimuthal locations, in which the initial and final polarization states are linearly polarized; (iii) when $\varepsilon \neq 0$, the ES-AV-HP-VOFs with m always produce $4m$ or $2m$ filaments, depending on the initial phase δ_0 ; and (iv) the filaments are more favorite to occur at azimuthal locations, in which the final polarization states after the nonlinear coupling tend to become into the linear polarization and have the smaller azimuthal gradient ($|\partial S_3/\partial \phi|$) of S_3 .

To understand the physics behind the collapsing behaviors, the azimuthal self-focusing model is very beneficial. The field collapse originates from the spatially variant refractive index change Δn and requires the existence of self-focusing nucleation(s) where the induced Δn must be local maximum. As is well known, the induced refractive index change Δn is directly proportional to both the local light intensity $I(\phi)$ and nonlinear refractive index coefficient $n_2(\phi)$. For the CS-AV-HP-VOFs ($\varepsilon = 0$), because its polarization states constitute a cylindrical symmetrical structure, the pre-focused intensity holds the axial symmetry, as shown in the first and second rows of Figs. 2, 4, and 6. The induced refractive index change Δn is only caused by the azimuthal-variant n_2 , whose value depends on the local polarization state. Accordingly, the energy tends to accumulate at the local position of linear polarization, because of $\Delta n^{\text{lin}} > \Delta n^{\text{ell}} > \Delta n^{\text{cir}}$ ($\Delta n^{\text{lin}} = 1.5\Delta n^{\text{cir}}$). For the ES-AV-HP-VOF ($\varepsilon \neq 0$), the elliptical-symmetry structure results in the intensity redistribution from the homogeneous distribution into the two separate strong peaks. Due to the synergy of the polarization structure and intensity distribution, the induced Δn strongly affects the nonlinear dynamic behaviors of the VOFs. Interestingly, the competition between the inhomogeneities of both intensity $I(\phi)$ and nonlinear refractive index coefficient $n_2(\phi)$ (originates from the azimuthal-variant polarization states) may cause the change of self-focusing nucleations, so the ES-AV-HP-VOFs ($\varepsilon \neq 0$) with different δ_0 will have a variety of collapsing behaviors.

Here we should point out that the quantity and locations of filamentation are dominated by the pre-collapse process, hence in all the above simulations we take into account the Kerr nonlinearity only, which is enough to elucidate the collapsing behaviors of the ES-AV-HP-VOFs. To further test, we also simulate the multiple filamentation when taking into account the higher-order nonlinearity important to the post-collapse process. Figure 8 shows the simulation results of the CS-AV-HP-VOF ($m = 1, \delta_0 = 0$) and the ES-AV-HP-VOFs

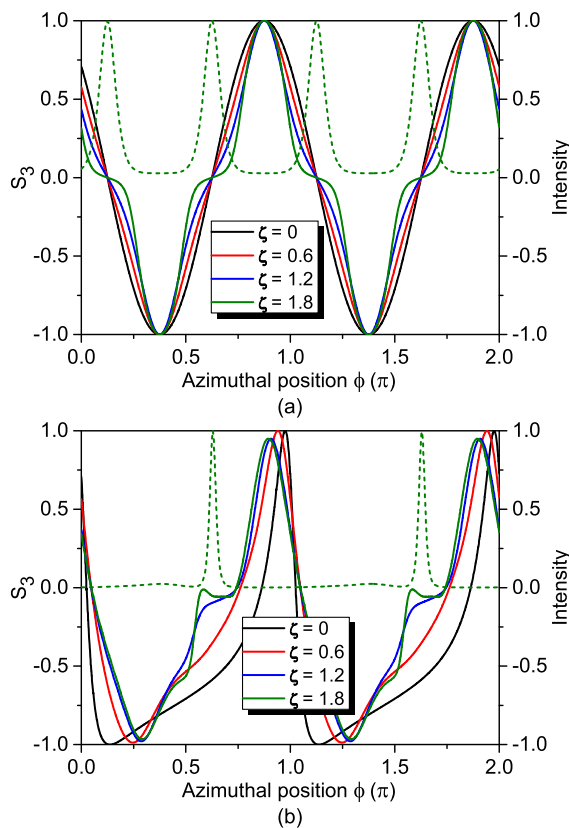


Fig. 7. Simulated evolution S_3 of the azimuthal-variant polarization states for the ES-AV-HP-VOFs ($m = 1$ and $\delta_0 = 3\pi/8$) with different eccentricity. (a) $\varepsilon = 0$ and (b) $\varepsilon \neq 0$.

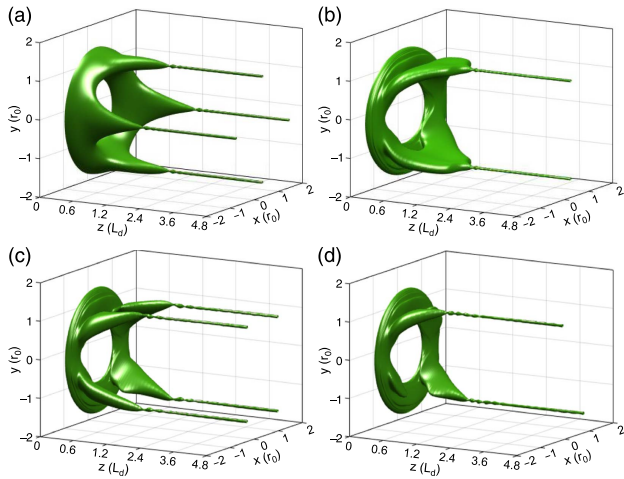


Fig. 8. Simulated collapsing evolution and multiple filamentation of the ES-AV-HP-VOFs. (a) CS-AV-HP-VOF with $m = 1$ and $\delta_0 = 0$; (b) ES-AV-HP-VOF with $m = 1$, $\varepsilon = 0.8$, and $\delta_0 = 0$; (c) ES-AV-HP-VOF with $m = 1$, $\varepsilon = 0.8$, and $\delta_0 = \pi/4$; and (d) ES-AV-HP-VOF with $m = 1$, $\varepsilon = 0.8$, and $\delta_0 = 3\pi/8$.

($m = 1, \varepsilon = 0.8$) with $\delta_0 = 0, \pi/4, 3\pi/8$. Beyond the collapse point, the sizes and the intensity of the filaments experience synchronous oscillations with the propagation distance. The filamentation patterns in the output face of the nonlinear medium are consistent with the pre-collapse points.

In addition, we also carried out some simulations under the spatial random noise with a level of 30% in amplitude, we keep the random noise, which follows a uniform distribution within a range of 30%. The simulation results (not shown here) confirm that our idea may produce the robust multiple filamentation against the random noise.

5. EXPERIMENTAL VERIFICATION

We follow the same method as [27] for creating the fs ES-AV-HP-VOFs required for the experimental verification. The used light source is a Ti:sapphire regenerative amplifier fs laser system (Coherent Inc.), which provides a fundamental Gaussian mode with a central wavelength of 800 nm, a pulse duration of 35 fs, and a repetition rate of 1 kHz. An achromatic 1/2-wave plate and a broadband polarized beam splitter were used to control the laser fluence input on the sample. Another achromatic 1/2-wave plate was used to change the polarization direction of the input fs laser into the vector field generation unit, where all the elements are achromatic to suppress the pulse broadening as much as possible. The created ES-AV-HP-VOFs have a “top-hat-like” spatial profile, excluding a central singularity caused by the polarization uncertainty, with a radius of 1.5 mm, a pulse energy of 6.0 mJ, and a pulse duration of ~ 65 fs.

To experimentally confirm our theoretical prediction and numerical simulations, all the required vector fields with different m , δ_0 , and ε were created by using the experimental scheme [27]. The created ES-AV-HP-VOFs were weakly pre-focused onto the CS₂ cell with a length of 30 mm, by an achromatic lens with a focal length of $f = 300$ mm. The intensity patterns of the field transmitted from the CS₂ cell are imaged on a

detector (Beamview, Coherent Inc.) using an achromatic lens with a focal length of $f = 60$ mm.

As shown in the first column of Fig. 9, corresponding to the CS-AV-HP-VOFs with ($m = 1, \varepsilon = 0$), the four filaments occur at the four azimuthal locations [$\phi(n) = (n + 1)\pi/2 - \delta_0$, where $n = 0, 1, 2, 3$] with the local linear polarization, as studied in [25]. As shown in the first and second rows with ($m = 1, \delta_0 = 0$), the four filaments reduce to the two filaments located at $\phi = \pi/2$ and $\phi = 3\pi/2$, as ε increases. As shown in the third and four rows with ($m = 1, \delta_0 = \pi/4$), however, the four filaments are still kept but are changed from a square into an elongated rectangle, as ε increases from $\varepsilon = 0$ to $\varepsilon = 0.8$. As shown in the fifth and sixth rows with ($m = 1, \delta_0 = 3\pi/8$), as ε increases, the four filaments also reduce to the two filaments located at near $\phi = 5\pi/8$ and $\phi = 13\pi/8$.

We also explore experimentally the collapsing behaviors of the ES-AV-HP-VOFs with $m = 2$. As examples, Fig. 10 shows the collapsing patterns of the ES-AV-HP-VOFs

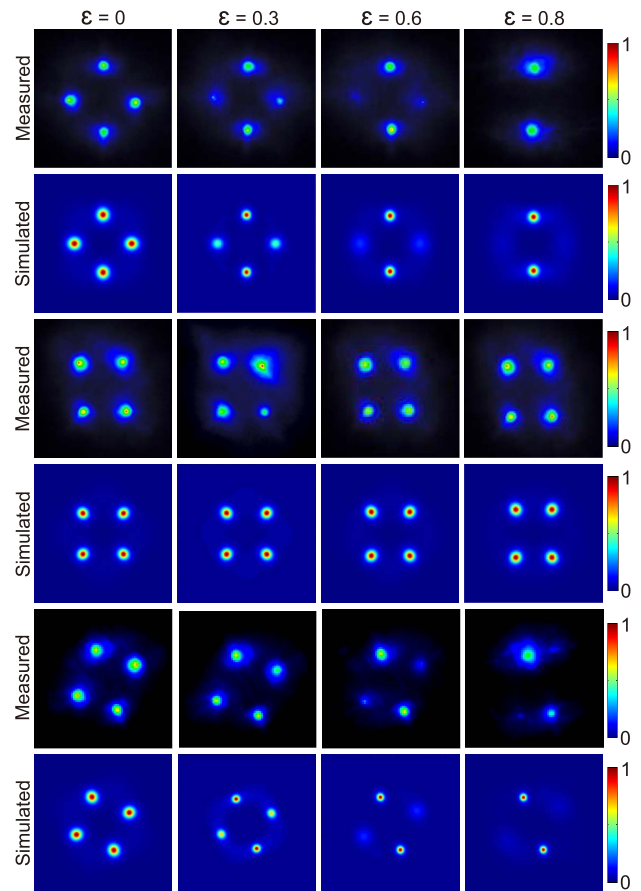


Fig. 9. Measured and simulated collapsing behaviors of the ES-AV-HP-VOFs ($m = 1$) with the different ε ($\varepsilon = 0, 0.6, 0.8$) in the Kerr medium. The first and second rows show the measured and simulated collapsing patterns of the ES-AV-HP-VOFs ($m = 1, \delta_0 = 0$), respectively. For comparison, the measured and simulated collapsing patterns of the ES-AV-HP-VOFs are also shown in the third and fourth rows for the case ($m = 1, \delta_0 = \pi/4$) and in the fifth and sixth rows for the case ($m = 1, \delta_0 = 3\pi/8$), respectively. The four columns (from the left to the right) correspond to four different ε ($\varepsilon = 0, 0.6, 0.8$).

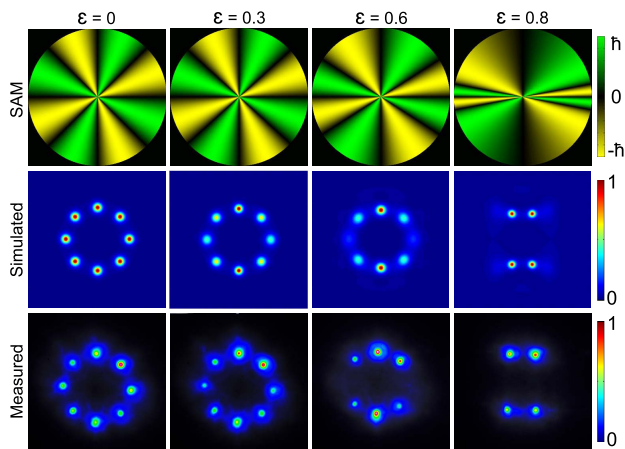


Fig. 10. SAM and the measured and simulated collapsing patterns of the ES-AV-HP-VOFs ($m = 2, \delta_0 = 0$) with different eccentricity ε ($\varepsilon = 0, 0.3, 0.6, 0.8$).

($m = 2, \delta_0 = 0$) for different values of ε . The first row shows the azimuthal distributions of the SAM (S_3) for $\varepsilon = 0, 0.3, 0.6, 0.8$. Clearly, the SAM (S_3) exhibits the change from the homogeneous distribution to the inhomogeneous one, as ε increases. As shown in the second (simulation) and third (experiment) rows, the ES-AV-HP-VOFs ($m = 2, \delta_0 = 0$) collapse into eight filaments for $\varepsilon = 0$, but four filaments occupying the four vertices of a rectangle (instead of a square) for $\varepsilon = 0.8$.

Clearly, the experimental results are in good agreement with the theoretical and numerical results for the ES-AV-HP-VOFs.

6. CONCLUSION

We have presented the theoretical prediction and performed the experimental evidence on the novel collapsing behaviors of the ES-AV-HP-VOFs in the self-focusing Kerr medium. Engineering the diversity of spatial distribution of polarization states is indeed a new approach to control the optical field collapse. The eccentricity, which describes the geometric configurations of the ES-AV-HP-VOFs, provides an additional degree of freedom assisting in controlling the variation of the SAM gradient of the hybrid polarization states and then the optical field collapse. Both theory and experiment demonstrate that the eccentricity ε , the topological charge m , and the initial phase δ_0 of the ES-AV-HP-VOFs can indeed control the locations and number of the filaments produced in the Kerr medium. When $\varepsilon = 0$, the ES-AV-HP-VOF with m degenerates into the CS-AV-HP-VOF with m , and the interaction with the Kerr medium will collapse into $4m$ filaments exhibiting a C_{4m} rotation symmetry. Due to the introduction of $\varepsilon \neq 0$, the axial symmetry of the optical field is broken, the ES-AV-HP-VOF with m and $\varepsilon \neq 0$ can collapse into $4m$ or $2m$ filaments depending on the initial phase δ_0 , but $4m$ filaments do not exhibit the C_{4m} rotation symmetry. Our idea may offer an alternative route to produce the controllable and robust multiple filamentation insensitive to the random noise, thereby facilitating the development of additional surprising applications.

Funding. National Key R&D program of China (13JCZDJC33800, 2017YFA0303700); National Natural Science Foundation of China (NSFC) (11534006, 11674184, 11774183); Natural Science Foundation of Tianjin City (16JCZDJC31300).

Acknowledgment. This work is supported by Collaborative Innovation Center of Extreme Optics.

REFERENCES

- P. A. Robinson, "Nonlinear wave collapse and strong turbulence," *Rev. Mod. Phys.* **69**, 507–574 (1997).
- C. D'Amico, A. Houard, M. Franco, B. Prade, A. Mysyrowicz, A. Couairon, and V. T. Tikhonchuk, "Conical forward THz emission from femtosecond-laser-beam filamentation in air," *Phys. Rev. Lett.* **98**, 235002 (2007).
- R. R. Alfano and S. L. Shapiro, "Emission in the region 4000 to 7000 Å via four photon coupling in glass," *Phys. Rev. Lett.* **24**, 584–587 (1970).
- P. Rohwetter, J. Kasparian, K. Stelmasczyk, Z. Hao, S. Henin, N. Lascoux, W. M. Nakaema, Y. Petit, M. QueiBer, R. Salamé, E. Salmon, L. Wöste, and J. P. Wolf, "Laser-induced water condensation in air," *Nat. Photonics* **4**, 451–456 (2010).
- F. Belgiorno, S. L. Cacciatori, M. Clerici, V. Gorini, G. Ortenzi, L. Rizzi, E. Rubino, V. G. Sala, and D. Faccio, "Hawking radiation from ultrashort laser pulse filaments," *Phys. Rev. Lett.* **105**, 203901 (2010).
- G. Fibich and B. Ilan, "Vectorial and random effects in self-focusing and in multiple filamentation," *Phys. D* **157**, 112–146 (2001).
- A. Couairon and A. Mysyrowicz, "Femtosecond filamentation in transparent media," *Phys. Rep.* **441**, 47–189 (2007).
- L. Bergé, S. Skupin, R. Nuter, J. Kasparian, and J. P. Wolf, "Ultrashort filaments of light in weakly ionized, optically transparent media," *Rep. Prog. Phys.* **70**, 1633–1713 (2007).
- R. Y. Chiao, E. Garmire, and C. H. Townes, "Self-trapping of optical beams," *Phys. Rev. Lett.* **13**, 479–482 (1964).
- P. L. Kelley, "Self-focusing of optical beams," *Phys. Rev. Lett.* **15**, 1005–1008 (1965).
- S. Varma, Y. H. Chen, and H. M. Milchberg, "Trapping and destruction of long-range high-intensity optical filaments by molecular quantum wakes in air," *Phys. Rev. Lett.* **101**, 205001 (2008).
- J. Kasparian and J. P. Wolf, "Physics and applications of atmospheric nonlinear optics and filamentation," *Opt. Express* **16**, 466–493 (2008).
- J. Kasparian, M. Rodriguez, G. Méjean, J. Yu, E. Salmon, H. Wille, R. Bourayou, S. Frey, Y. B. André, A. Mysyrowicz, R. Sauerbrey, J. P. Wolf, and L. Wöste, "White-light filaments for atmospheric," *Science* **301**, 61–64 (2003).
- Y. Ren, M. Alshershby, Z. Hao, Z. Zhao, and J. Lin, "Microwave guiding along double femtosecond filaments in air," *Phys. Rev. E* **88**, 013104 (2013).
- J. Zhao, L. Guo, W. Chu, B. Zeng, H. Gao, Y. Cheng, and W. Liu, "Simple method to enhance terahertz radiation from femtosecond laser filament array with a step phase plate," *Opt. Lett.* **40**, 3838–3841 (2015).
- A. Camino, Z. Hao, X. Liu, and J. Lin, "High spectral power femtosecond supercontinuum source by use of microlens array," *Opt. Lett.* **39**, 747–750 (2014).
- Z. Jin, J. Zhang, M. H. Xu, X. Lu, Y. T. Li, Z. H. Wang, Z. Y. Wei, X. H. Yuan, and W. Yu, "Control of filamentation induced by femtosecond laser pulses propagating in air," *Opt. Express* **13**, 10424–10430 (2005).
- A. Dubietis, G. Tamošauskas, G. Fibich, and B. Ilan, "Multiple filamentation induced by input-beam ellipticity," *Opt. Lett.* **29**, 1126–1128 (2004).
- T. D. Grow and A. L. Gaeta, "Dependence of multiple filamentation on beam ellipticity," *Opt. Express* **13**, 4594–4599 (2005).
- T. Pfeifer, L. Gallmann, M. J. Abel, D. M. Neumark, and S. R. Leone, "Circular phase mask for control and stabilization of single optical filaments," *Opt. Lett.* **31**, 2326–2328 (2006).

21. V. P. Kandidov, N. Aközbeke, M. Scalora, O. G. Kosareva, A. V. Nyakk, Q. Luo, S. A. Hosseini, and S. L. Chin, "A method for spatial regularisation of a bunch of filaments in a femtosecond laser pulse," *Quantum Electron.* **34**, 879–880 (2004).
22. Z. Q. Hao, K. Stelmaszczyk, P. Rohwetter, W. M. Nakaema, and L. Woeste, "Femtosecond laser filament-fringes in fused silica," *Opt. Express* **19**, 7799–7806 (2011).
23. Z. Q. Hao, J. Zhang, T. T. Xi, X. H. Yuan, Z. Y. Zheng, X. Lu, M. Y. Yu, Y. T. Li, Z. H. Wang, W. Zhao, and Z. Y. Wei, "Optimization of multiple filamentation of femtosecond laser pulses in air using a pinhole," *Opt. Express* **15**, 16102–16109 (2007).
24. W. Walasik and N. M. Litchinitser, "Dynamics of large femtosecond filament arrays: possibilities, limitations, and trade-offs," *ACS Photonics* **3**, 640–646 (2016).
25. S. M. Li, Y. N. Li, X. L. Wang, L. J. Kong, K. Lou, C. H. Tu, Y. J. Tian, and H. T. Wang, "Taming the collapse of optical fields," *Sci. Rep.* **2**, 1007 (2012).
26. S. M. Li, Z. C. Ren, L. J. Kong, S. X. Qian, C. H. Tu, Y. N. Li, and H. T. Wang, "Unveiling stability of multiple filamentation caused by axial symmetry breaking of polarization," *Photonics Res.* **4**, B29–B34 (2016).
27. X. L. Wang, Y. N. Li, J. Chen, C. S. Guo, J. P. Ding, and H. T. Wang, "A new type of vector fields with hybrid states of polarization," *Opt. Express* **18**, 10786–10795 (2010).
28. G. Fibich and A. L. Gaeta, "Critical power for self-focusing in bulk media and in hollow waveguides," *Opt. Lett.* **25**, 335–337 (2000).
29. G. Agrawal, *Nonlinear Fiber Optics* (Academic, 2012).